J. Vis. Commun. Image R. 23 (2012) 697–704

Contents lists available at SciVerse ScienceDirect

J. Vis. Commun. Image R.

journal homepage: www.elsevier.com/locate/jvci

Reducing frequency-domain artifacts of binary image due to coarse sampling by repeated interpolation and smoothing of Radon projections

Peizhen Zhang [a,b], Shuozhong Wang [a,*], Runtian Wang [c]

[a] School of Communication and Information Engineering, Shanghai University, Shanghai 200072, China
[b] School of Information, Guangdong Ocean University, Zhanjiang 524088, China
[c] Shanghai Acoustics Laboratory, Chinese Academy of Sciences, Shanghai 200032, China

ARTICLE INFO

Article history:
Received 18 June 2011
Accepted 2 April 2012
Available online 9 April 2012

Keywords:
Discrete Radon transform
Radon projection
Fourier slice theorem
Polar coordinate interpolation
Low-pass filtering
Fourier diffraction theorem
Acoustic tomography
Interpolation-smoothing-decimation

ABSTRACT

We develop a method to calculate 2D spectrum of a binary image with better quality than that obtained via direct 2D-FFT. With FFT, jagged edges of objects due to coarse sampling introduce artifacts into the frequency domain, especially in the high-frequency area. With the proposed method, Radon projections of the binary image along lines at different viewing angles are calculated. Each projection is extended by interpolation, then smoothed and decimated. The interpolation–smoothing–decimation operation is repeated several times to reduce ruggedness and improve quality of the Radon projections considerably. One-dimensional FFT of each refined Radon projection is calculated, resulting in a set of frequency-domain samples distributed on a polar coordinate system. These samples are interpolated onto a Cartesian grid to give the required 2D spectrum of the sampled binary image. Numerical computations on several objects show that the method can provide significant improvement to the spectrum as compared with direct 2D-FFT.

1. Introduction

The present work is motivated by a recent study on the reversed use of the *Fourier diffraction theorem* to predict patterns of acoustic scattering [1]. In that work, we consider a 2D sound scattering problem in which an infinitely long cylindrical object is immersed in water and insonified by a plane sound wave. The incident wave propagates towards the cylinder, perpendicular to the axis. The cross-sectional distributions of acoustical properties, *i.e.*, refraction indices, of the object and the water form a binary image. The Fourier diffraction theorem, which is the foundation of acoustic tomography [2], states that the forward- and backward-scattered field distributions correspond to 1D inverse Fourier transform of spectral values taken along a pair of half-circles in the 2D Fourier transform of the image. The values taken on the half-circles are used to efficiently calculate the field projections using 1D inverse Fourier transform.

In numerical implementations, the binary image in the spatial domain is sampled on a grid, and 2D DFT is calculated to obtain the frequency domain representation of the object. Jagged edges of the sampled object cause significant errors in the 2D spectrum. Especially, spectral values in high frequency regions may be completely corrupted. This leads to intolerable errors in the derived scattered sound values. To solve the problem, an effective method is needed to reduce the sampling-caused spectral artifacts in order to improve accuracy of the generalized projections derived from the 2D spectrum.

Research has been done to correct spectral errors in the discrete Fourier transform domain for various purposes. Zhao et al. [3] study a time reversal method and propose a de-trending algorithm to reduce phase errors at different noise levels. Zhu et al. [4] use the Parseval's theorem to derive two expressions for line spectra, and correct amplitudes by averaging multiple points in the DFT sequence. Ding and Ming [5] develop a phase-difference method to correct frequencies and phases of spectral peaks. The frequency and phase are corrected using the phase difference between spectral lines, and amplitude modified using the spectrum of a window function.

To improve the spectrum of cross-sectional images in the acoustic scattering applications, one might consider increasing spatial resolution by up-sampling the object in the space domain, or using zero-padding to calculate 2D-FFT. In [6], Mueller and Nguyen integrate several interpolation methods and use region classification to choose a suitable method for a particular region. Zhang and Wu [7] propose an edge-guided non-linear interpolation approach by directional filtering and data fusion based on minimum MSE estimation to reduce computation cost. Interpolation of binary images has also been addressed. For example, Ledda et al. use interpolation and morphological hit-miss transform to reduce

* Corresponding author.
E-mail addresses: zpzhen7242@163.com (P. Zhang), shuowang@shu.edu.cn (S. Wang), wangrunt@126.com (R. Wang).

1047-3203/$ - see front matter © 2012 Elsevier Inc. All rights reserved.
http://dx.doi.org/10.1016/j.jvcir.2012.04.001

jagged edges of binary images to magnify logos, diagrams, texts and cartoons [8]. In these methods, jagged image edges are smoothed in an enlarged image. However, using these methods, the spectra often contain artifacts such as ringing, aliasing, and blocking, and therefore are unsuitable for space-domain projection reconstruction in our applications.

Up-sampling and zero-padding either increase computation cost and memory requirements with some remaining errors, or simply cannot eliminate high-frequency artifacts as will be shown in Section 4.2. In this paper, we propose an alternative method based on interpolation of Radon projections to keep a low space-domain sampling rate and provide much improved high frequency performance.

In Section 2, an operation of repeated interpolation/smoothing is described. Interpolation is performed on the projection of the object obtained from the discrete Radon transform, hence the name *Radon projection*, followed by low-pass filtering and decimation to produce a smoother projection. This process is repeated several times to achieve adequate accuracy with the same spatial sampling rate. One-dimensional Fourier transform of the smoothed projections gives improved frequency domain samples on radials of the polar coordinates in the frequency domain. In Section 3, two-dimensional conversion in the Fourier domain is carried out to map the polar samples onto a Cartesian grid so as to obtain improved 2D discrete Fourier transform of the jagged binary image. Results of numerical computation are presented in Section 4 to show effectiveness of the method. Section 5 concludes the paper.

2. Improving Radon projection by interpolation and low-pass filtering

2.1. Discrete Radon projection

Given an object represented by an $N \times N$ array $I(n_1,n_2)$ in a two dimensional space, the discrete Radon projection is defined by summing the samples of $I(n_1,n_2)$ along lines at angle θ with the positive direction of x-axis [9]

$$p_\theta(k) = \begin{cases} \mathcal{R}(\{y = x\tan\theta + k\}, I) = \sum_{n_1=-N/2}^{N/2-1} I_1(n_1, n_1\tan\theta + k), \\ \quad \theta \in [-\pi/4, \pi/4],\ n_1 = -N/2, \ldots, N/2-1, \\ \quad \text{basically horizontal} \\ \mathcal{R}(\{x = y\cot\theta + k\}, I) = \sum_{n_2=-N/2}^{N/2-1} I_2(n_2\cot\theta + k, n_2), \\ \quad \theta \in [\pi/4, 3\pi/4],\ n_2 = -N/2, \ldots, N/2-1, \\ \quad \text{basically vertical} \end{cases} \tag{1}$$

where $\mathcal{R}$ indicates the discrete Radon transform, and $k = \lceil(-N/\sqrt{2})\rceil, \ldots, 0, \ldots, \lceil(N/\sqrt{2}-1)\rceil$ in which $\lceil\cdot\rceil$ means upward rounding. Both I_1 and I_2 are derived from the object image $I(n_1,n_2)$:

$$\begin{cases} I_1(n_1,y) = \sum_{n_2=-N/2}^{N/2-1} I(n_1,n_2)D(y-n_2) \\ I_2(x,n_2) = \sum_{n_1=-N/2}^{N/2-1} I(n_1,n_2)D(x-n_1) \end{cases} \tag{2}$$

where D is the Dirichlet kernel:

$$D(k) = \frac{\sin(\pi k)}{(2N+1)\sin[\pi k/(2N+1)]} \tag{3}$$

The Fourier slice theorem states that Fourier transform of the projection gives values on a slice in the 2D Fourier transform of the object image as depicted in Fig. 1 [10]. Due to jaggedness in the discrete representation of the object, direct use of the projection to produce its spectrum will result in intolerable errors. Our aim is to improve quality of the Radon projection.

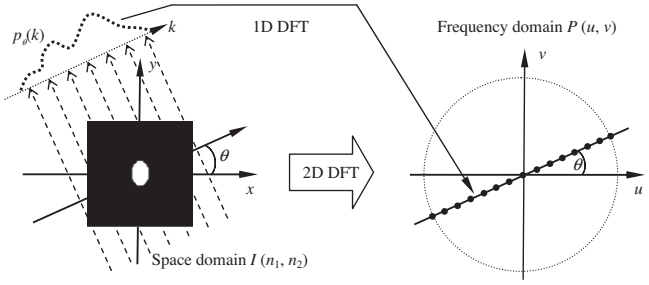

Fig. 1. Radon projection and Fourier slice theorem.

2.2. Improving Radon projection by repeated interpolation and low-pass filtering

To smooth a discrete Radon projection, the first step is to expand the initial projection sequence using the piecewise cubic Hermite interpolation (PCHI) [11]. In the kth interval, denoted by $[k,k+1]$, the PCHI polynomial is

$$\begin{aligned} p_\theta(x) = {} & [3(x-k)^2 - 2(x-k)^3]p_\theta(k+1) + [1 - 3(x-k)^2 \\ & + 2(x-k)^3]p_\theta(k) + (x-k)^2(x-k-1)d_{k+1} \\ & + (x-k)(x-k-1)^2 d_k, \quad k = 1,2,\ldots,K \end{aligned} \tag{4}$$

where $K = \sqrt{2}N$ Let L be the number of inserted values between the kth and $(k+1)$th samples so that $x = k + l/(L+1)$, where $l = 0,1,\ldots,L$. This way, the length of a projection is extended to $W = (\sqrt{2}N-1)(L+1)$. Let d_k denote the slope at the sample k. If $[p_\theta(k+1) - p_\theta(k)]$ and $[p_\theta(k) - p_\theta(k-1)]$ have opposite signs or if either of them is zero, we set $d_k = 0$. Otherwise d_k is calculated as follows:

$$d_k = 2\left[\frac{1}{p_\theta(k) - p_\theta(k-1)} + \frac{1}{p_\theta(k+1) - p_\theta(k)}\right]^{-1} \tag{5}$$

Denote the interpolation-extended projection as $q_\theta(w)$, $w = 1,2,\ldots,W$. Next, use an Sth order finite impulse response (FIR) filter to smooth the interpolated projections:

$$q'_\theta(w) = \sum_{s=1}^{S} h(s)q_\theta(w-s), \quad w = 0,1,2,\ldots,W \tag{6}$$

The filter weights $h(s)$ are defined as a Kaiser window [12].

Decimation is then performed by taking every $(L+1)$th sample to restore the length of projection back to that of the original sequence, K:

$$p_\theta^{(1)}(k) = \begin{cases} q'_\theta[(L+1)(k-1)], & k = 2,3,\ldots,K \\ q'_\theta(k), & k = 1 \end{cases} \tag{7}$$

This is the result of the first cycle of the operations as marked in the superscript, which is an improved version of $p_\theta(k)$. Repeating the interpolation–smoothing–decimation steps, quality of the projection is progressively improved. We compute the following quantity representing the mean square difference (MSD) between two consecutive modified projections:

$$d^{(t)} = \sqrt{\frac{1}{K}\sum_{k=1}^{K}\left[p_\theta^{(t)}(k) - p_\theta^{(t-1)}(k)\right]^2} \tag{8}$$

The proper number of repetitions may be determined by calculating $d^{(t)}$ with increasing t. We call the final $p'_\theta(k)$ as the *smoothed Radon projection*, or simply the *smoothed projection*. Progressive improve-

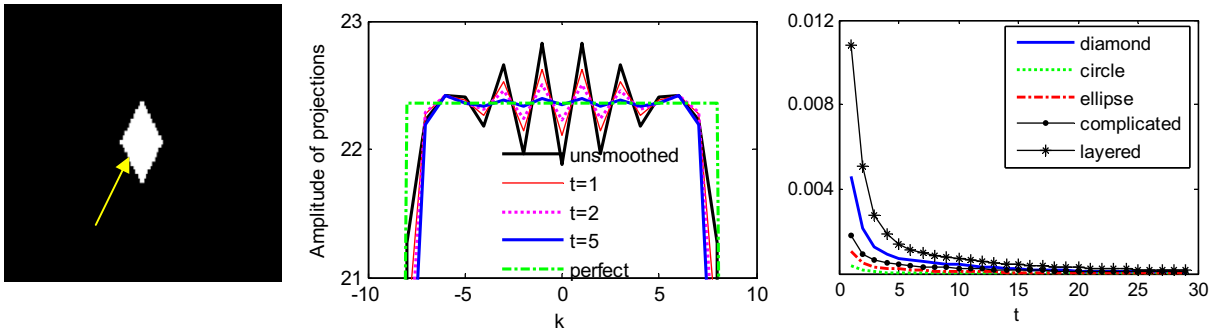

(a) Object and incident wave (b) Projections with different t values (c) MSD of 5 objects as functions of t

Fig. 2. Smoothed Radon projections obtained with different numbers of repeated operations. The wavelength $\lambda = 1$ m, and spatial sampling interval = 0.1 m. In (c), five objects of different shapes are considered, including one with a more complicated shape and another having a layered structure (see Fig. 10).

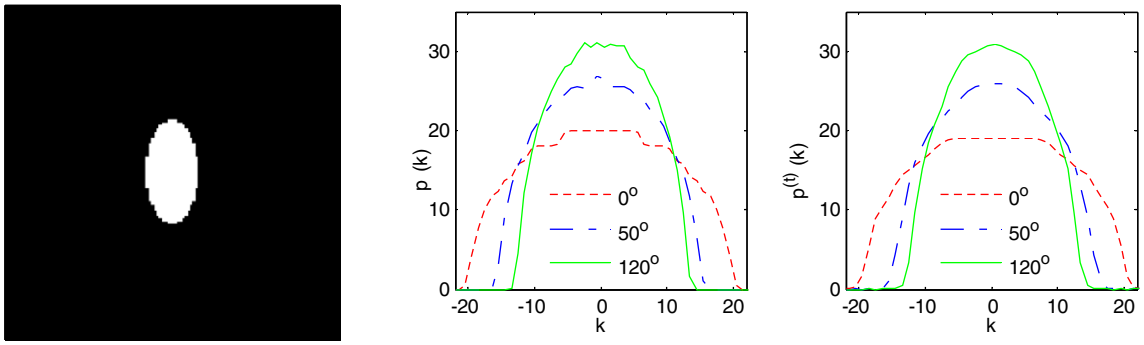

(a) Cross-sectional image (b) Unsmoothed Radon projections in 3 directions (c) Smoothed results

Fig. 3. Comparison between discrete Radon projections and their smoothed versions of an elliptical cylinder in water.

ment of the repeated operations is illustrated in Fig. 2, in which (a) shows a diamond-shaped object insonified by a sound wave at 63°, parallel to the two sides, and (b) gives an unsmoothed Radon projection and improved results with different numbers of interpolation/filtering/decimation repetitions. The dash-dotted green line[1] indicates the perfect projection. Fig. 2(c) shows MSD of the projections as a function of the repetition times, t. Objects of different shapes have been tested, including one with a more complicated shape and another having a layered structure as shown in Fig. 10. It is observed that precision of the calculated projections is improved with increasing t. We find that $t = 5$ is a reasonable trade-off between quality of the projection and the computation load.

2.3. Numerical examples

Consider two infinitely-long cylindrical objects, with the cross-sections being an ellipse with the axes of 1 m and 2 m, and a diamond with two diagonals of 1 m and 2 m, and the vertex angle = 53°. Assume wavelength of the incident sound wave is 1 m and choose a grid interval $\delta = 0.1$ m, which meets the condition of sufficient spatial sampling used in numerical field computation methods such as finite difference time domain (FDTD) method [13]. Choose a computation domain with 129×129 pixels (12.9×12.9 m^2), and use the sound refraction index to construct a cross-sectional binary image.

[1] For interpretation of color in Figs. 2, 9, and 13, the reader is referred to the web version of this article.

Let the incident plane sound wave propagate in the directions 0°, 50° and 120° respectively, and calculate the unsmoothed discrete Radon projections and their smoothed versions with $t = 5$. Figs. 3 and 4 present comparisons between the unsmoothed and smoothed projections of different objects. Note the jagged edges of the objects and the resulting jagged curves of the unsmoothed projections. The obtained projections are clearly smoother.

As the purpose is to obtain good spectra based on coarsely sampled object profiles, we demonstrate the achieved improvement in the frequency domain. Fig. 5 presents the 1D Fourier transforms of the unsmoothed and smoothed projections for the above three objects. Here a plane sound wave is assumed to propagate along $\theta = 40°$. Compared with 1D-FFT of perfect projection, the improvement in the spectra of the smoothed projection is obvious.

3. Two-dimensional interpolation of Fourier domain samples

In this section, we use the smoothed Radon projections to produce a spectrum of the object's cross-section with satisfactory quality. Suppose we have obtained M such projections within 180°. The choice of M depends on the image size. In general, a large image requires a large M to ensure sufficient sampling in off-center regions. One-dimensional Fourier transform of the smoothed projections along the directions $\theta \in [0°, 180°)$ can be obtained:

$$P_\theta(r) = \sum_{k=0}^{K-1} p_\theta(k) \exp\left(\frac{-j2\pi kr}{K}\right), \quad r = 1, 2, \ldots, K; \ \theta = 0, 1, \ldots, M \tag{9}$$

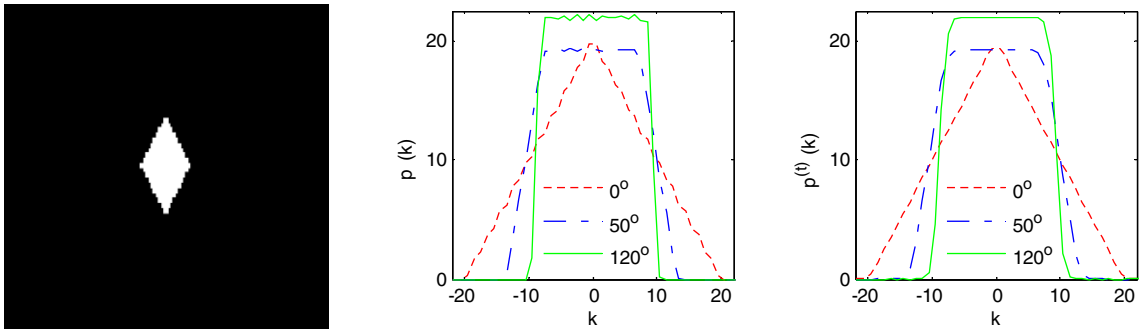

(a) Cross-sectional image (b) Unsmoothed Radon projections in 3 directions (c) Smoothed results

Fig. 4. Comparison between discrete Radon projections and their smoothed versions of a diamond cylinder in water.

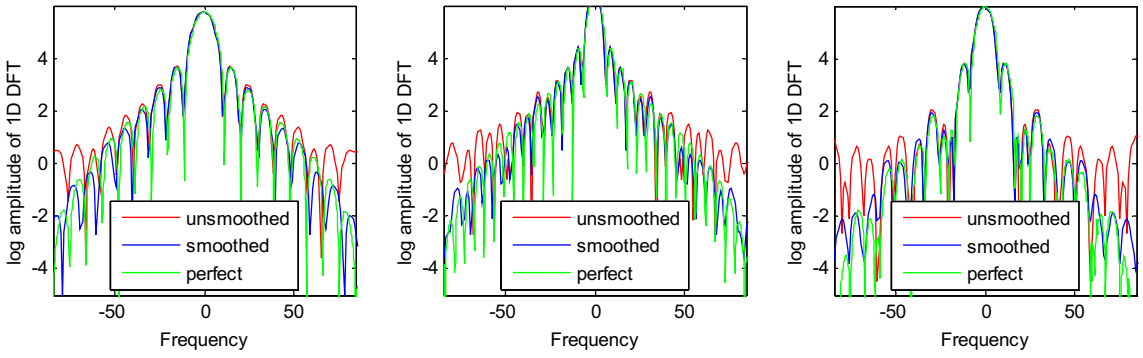

(a) Circle (b) Ellipse (c) Diamond

Fig. 5. Comparison of 1D FFT from the original unsmoothed, smoothed, and perfect Radon projections of different objects, with a sound wave incident at 40°.

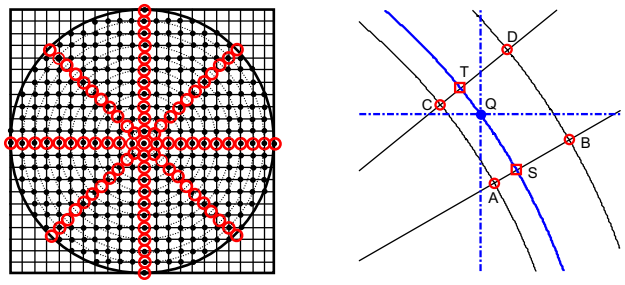

(a) Samples on polar and Cartesian coordinates (b) A zoomed-in view

Fig. 6. Interpolation in the 2D Fourier transform domain.

For notational clarity, the superscription representing the repetition number of the interpolation-smoothing-decimation operations is omitted, which is 5 in the present work.

According to the Fourier slice theorem as illustrated in Fig. 1, Eq. (9) produces a total of $M \cdot K$ spectral samples of the object, distributed on radials of M different angles in a polar coordinate system. In Fig. 6(a), samples on the radial lines with $\theta = 0°$, 45°, 90°, and 135° are shown schematically by small circles. In the polar coordinate system, the radial axis represents frequencies [14]. The angular increment equals 180 divided by M. In the following computation, we choose $M = 180$ with an increment of 1°. Thus, the discrete polar coordinate grid is:

$$\begin{cases} \gamma_k = \pi k/K, & k = -K/2, \ldots, 0, \ldots, K/2 - 1 \\ \theta = 0, 1, \ldots, 179 \end{cases} \tag{10}$$

For a higher spectral resolution, the projections may be extended by zero-padding to a length $K' = TK$, where T is the zero-padding factor, and K equals $\sqrt{2}N$. Accordingly, the 2D Cartesian grid is oversampled to give the size $K' \times K'$. In Section 4, we will show that letting $T = 2$ and using linear interpolation can provide adequate accuracy for our purpose.

We now convert the samples on the radials onto a grid to give $P(u, v)$, u, $v = -K'/2, 2, \ldots, K'/2 - 1$, the Cartesian coordinate representation of the 2D DFT of the object image $I(n_1, n_2)$. Referring to Fig. 6(a), since the spectral samples directly obtained from the smoothed Radon projections are only available inside a circle, we interpolate the samples to a grid within the circular area.

To find the spectral value at point Q on the Cartesian system, see Fig. 6(b), we need to identify the four neighboring points that are already known on the polar system. The polar coordinates of Q are calculated from the Cartesian coordinates (u, v):

$$\begin{cases} r' = \sqrt{u^2 + v^2} \\ \theta' = 180 \times \arctan(u/v)/\pi \end{cases} \tag{11}$$

Therefore the four neighbors of Q on the polar coordinates are $A(\lfloor r' \rfloor, \lfloor \theta' \rfloor)$, $B(\lfloor r' \rfloor + 1, \lfloor \theta' \rfloor)$, $C(\lfloor r' \rfloor, \lfloor \theta' \rfloor + 1)$, and $D(\lfloor r' \rfloor + 1, \lfloor \theta' \rfloor + 1)$ where $\lfloor \cdot \rfloor$ is a downward rounding operator. Linear interpolation is performed to get the spectral values at points S and T:

$$\begin{cases} P_S = (r' - \lfloor r' \rfloor) \cdot P_B + (\lfloor r' \rfloor + 1 - r') \cdot P_A \\ P_T = (r' - \lfloor r' \rfloor) \cdot P_D + (\lfloor r' \rfloor + 1 - r') \cdot P_C \end{cases} \tag{12}$$

Finally, the required spectral value at point Q is obtained:

$$P_Q = [1 - (\theta' - \lfloor \theta' \rfloor)]P_S + (\theta' - \lfloor \theta' \rfloor)P_T \tag{13}$$

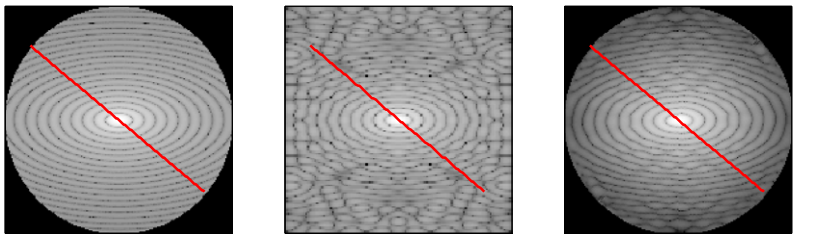

(a) Sampled analytical result (b) 2D-FFT of sampled image (c) Result of proposed method

Fig. 7. Spectral magnitude of an elliptical cross-section image.

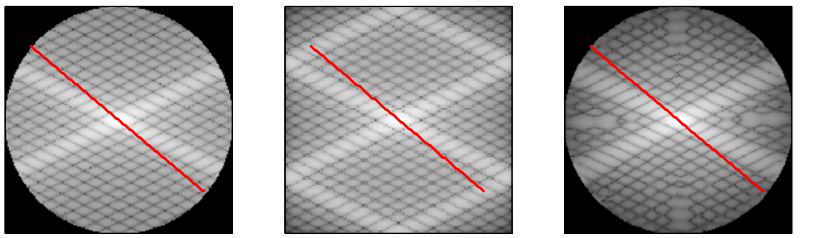

(a) Sampled analytical result (b) 2D-FFT of sampled image (c) Result of proposed method

Fig. 8. Spectral magnitude of a diamond-shaped cross-section image.

4. Numerical results

4.1. Computed spectra and reconstructed projections

We have done numerical computations for cylinders with elliptic and diamond-shaped cross-sections. The results are shown in Figs. 7 and 8. In each figure, we show the spectral magnitudes obtained in the following three ways:

1. Analytically calculate the Fourier transform from the functional form of the object, $I(x,y)$, and sample the spectral magnitudes on a Cartesian grid, thus obtaining *perfect projections* from the Fourier spectrum. The functional forms of the 2D spectra are given in the appendix.
2. Sample the image $I(x,y)$ with a spatial interval $\delta = 0.1$ m to get $I(n_1\ n_2)$, and calculate the direct 2D-FFT.
3. Calculate and plot the spectral magnitudes using the proposed scheme with five repetitions and zero-padding factor $T = 2$.

Note that all the spectral magnitudes are plotted in a logarithmic scale to compress the dynamic range for display clarity. It is observed that, with direct sampling and 2D-FFT, the resulting spectra contain unacceptable errors, while the quality of the spectra obtained by using the proposed method is much more satisfactory.

Inverse 1D FFT of the samples taken from the red lines reproduces spatial domain projections in the corresponding direction as shown in Fig. 9, which further visualizes the achieved improvements. It is clear that the proposed method can reproduce projections very close to the perfect ones, while the direct 2D-FFT (uncorrected) method produces poor, even erroneous, results.

More complicated objects such as those with more complicated shapes or having interior structures shown in Fig. 10 can also be treated. As analytical expressions of the spectra are unavailable, the reconstructed projections obtained by using the proposed method are compared with Radon projections calculated from the smooth versions of these objects. Clearly, the corrected projections of the coarsely sampled objects are close to the Radon projections of the smooth objects, while the projections of the coarsely-sampled objects based on the direct 2D-FFT method are erroneous. Gray-scale images are irrelevant to the objective of the present study, and therefore not considered.

We now calculate mean absolute errors of the reconstructed projections of different viewing angles. Fig. 11 shows the results in the range of $[0°, 180°]$ with a $5°$ interval for elliptic and diamond

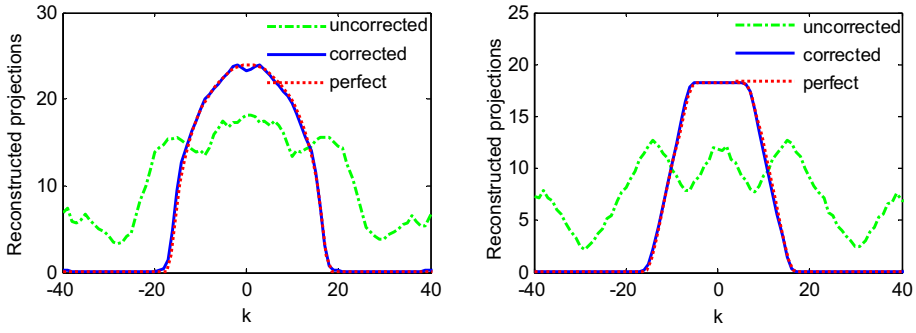

(a) Ellipse (b) Diamond

Fig. 9. Comparison of projections reconstructed from the 2D spectrum along 40° along the red lines shown in Figs. 7 and 8. Each plot contains three curves obtained from the uncorrected spectrum resulted from direct 2D-FFT, the spectrum corrected with the proposed method, and the analytically calculated spectrum, respectively.

(a) Cross-sectional image of complex shape object (b) Cross-sectional image of layered object

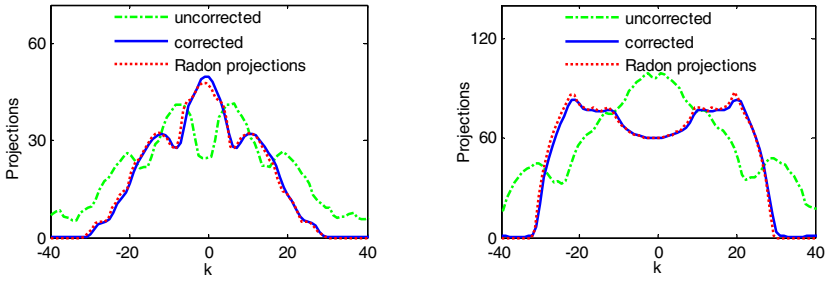

(c) Reconstructed projections of the object in (a) (d) Reconstructed projections of the object in (b)

Fig. 10. Reconstructed projections of more complicated objects in the direction of 40°. Each of the plots in (c) and (d) contains three curves obtained from the uncorrected spectrum resulted from direct 2D-FFT and the proposed method, and Radon projections from smooth objects respectively.

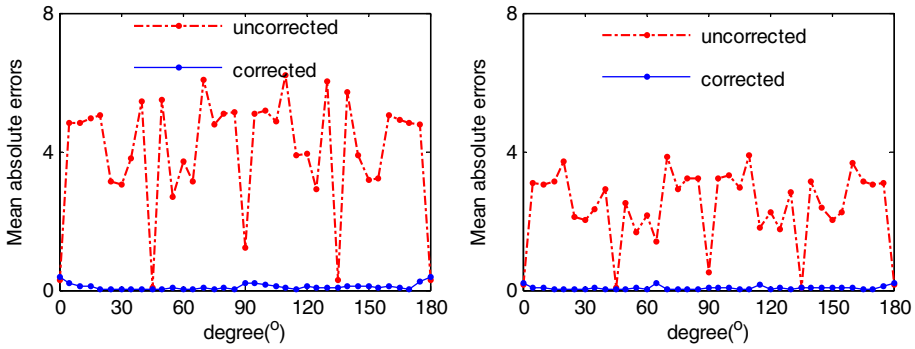

(a) Ellipse (b) Diamond

Fig. 11. Mean absolute errors of each view. Each plot obtained by mean absolute errors of reconstructed projections from the uncorrected spectrum using the direct 2D-FFT method and the proposed method, respectively.

objects, which is generally independent of the direction. Mean absolute errors of the direct 2D-FFT method as given in the same plots are significantly higher and fluctuate with the changing angle due to the edge jaggedness.

4.2. Comparison of spectral quality with zero-padding and up-sampling

As is well known, smoothness of the spectra can be improved by increasing spatial samples either with zero-padding or up-sampling in direct 2D-FFT. We now show that both of these are inferior to the proposed method. Fig. 12 shows projections reconstructed by using the proposed, zero-padding with a factor F, and up-sampling with a factor S, respectively. The sound wavelength is assumed to be 1 m, the elliptic object has two axes of 1 m and 2 m, and the incident angle is 40°. We make the following observations on the computed results.

(1) For the proposed method, a repetition number 5 is used in interpolation-smoothing-decimation steps, and different values of T are tested. With $T = 2$, the reconstructed result is already smooth enough and very close to the perfect projection. Increasing the T value makes little improvement.
(2) For the zero-padded 2D-FFT method, the reconstructed projections are clearly poorer than those of the proposed approach. Only with a quite large zero-padding factor F can acceptable results be obtained. But in this case, the computation load is greatly increased. Although FFT of a large data array may not take a terribly long time, the memory requirement can become prohibitive. For example, when $F = 8$, the memory size required in a 2D case is 64 times as large, and becomes 512 times in a 3D case.
(3) When the projection is calculated from the center part of the spectrum that is improved by space-domain up-sampling, the result is still erroneous because the spectral resolution is low no matter how large an up-sampling factor S is used, see Fig. 12(c). To solve the problem, we pad zeros after

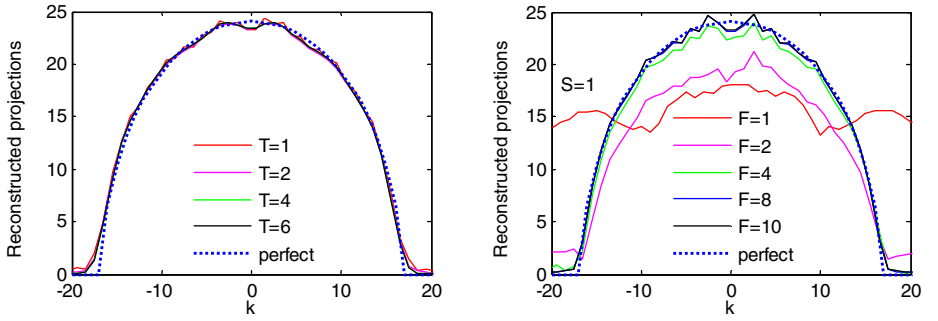

(a) Proposed method (b) 2D-FFT with only zero-padding

(c) 2D-FFT with only up-sampling (d) 2D-FFT with up-sampling plus zero-padding

Fig. 12. Comparison on accuracy of reconstructed projections. *T* is the zero-padding factor in the polar-Cartesian interpolation, *F* is the zero-padding factor in 2D-FFT, and *S* is the up-sampling factor before 2D-FFT.

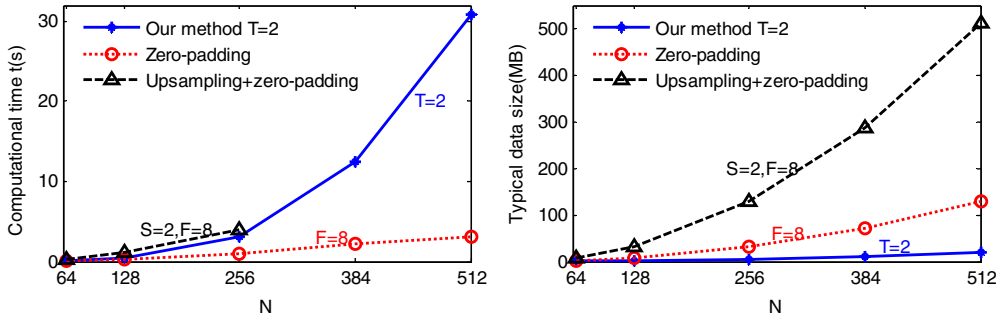

(a) Computation time (b) Sizes of typical data

Fig. 13. Comparison of computation cost between the proposed method and zero-padding/up-sampling 2D-FFT.

up-sampling and before 2D-FFT to increase the spectral resolution. The results are shown in Fig. 12(d) with $S = 2$. They are similar to (b) except that the curves are smoother.

4.3. Computation cost

Now we consider computation cost of the proposed scheme in terms of computation time and memory requirements, and compare it with 2D-FFT using zero-padding and up-sampling. We use a computer with a Core 2 CPU running at 3 GHz and a 4 GB RAM in the computation.

Fig. 13(a) shows computation time needed by using the three methods. The abscissa N is the number of pixels in one side of the square computation area. The zero-padding method with a factor of $F = 8$ (dotted red line) consumes the shortest time. When the computation area is small, the time needed for the proposed method (with $T = 2$) is slightly less than that of 2D-FFT with up-sampling plus zero-padding ($S = 2$, and $F = 8$). As N becomes larger, computation time of 2D-FFT with zero-padding increases slowly, while that of the proposed method rises quite steeply. In fact, the most time-consuming operation in the proposed method is the polar-Cartesian interpolation. Computation time of the up-sampling plus zero-padding method for $N > 256$ is not shown in the plot as an out-of-memory error occurs.

To show advantage of the proposed method in terms of memory requirements, we compare sizes of typical data used in the computation of the three methods in Fig. 13(b). The proposed method uses the least memory space because the data arrays are not enlarged and the interpolation–smoothing–decimation operation is one dimensional. The zero-padding and up-sampling plus zero-padding methods need to expand 2D arrays during the computation, and thus require much larger memory spaces.

5. Conclusions

The jagged edge of a binary image leads to errors in the discrete Fourier transform, especially in high frequency regions. When used

in fast prediction of sound scattering characteristics as described in [1], such errors can seriously affect accuracy of the results. In this work, we propose a method to calculate the 2D spectrum of a coarsely sampled binary image based on Radon projections and conversion of polar-coordinate samples onto the Cartesian system in the frequency domain. Quality of the Radon projections is substantially improved via repeated operations of interpolation, smoothing, and decimation. Consequently, a refined spectrum is obtained. The improved Fourier domain samples are available within a circular area. Numerical computation shows that the resulting spectra for several regular-shaped objects are very close to the sampled analytical spectra. Also, reproduced space-domain projections have high precision as compared to the projections directly calculated from the functional forms of the objects. The scheme is applicable to binary images of any shape.

Compared to 2D-FFT with zero-padding or up-sampling plus zero-padding, the proposed method consumes more computation time, primarily due to the polar-Cartesian interpolation. However, in terms of memory space requirements, the proposed method has clear advantage over the zero-padding/up-sampling methods, making it practical to use an ordinary desk-top computer for a fairly large computation domain.

We have mainly considered binary images, and used two types of simple shaped objects to show effectiveness of the method: circle and ellipse with smooth profiles and diamond with straight edges and sharp corners. More complicated objects such as those with different shapes or interior structures of more than two levels can also be treated provided the surrounding medium is uniform. Gray-scale images are under further study.

Acknowledgment

This work was supported by the Natural Science Foundation of China under the Grant No. 61071187.

Appendix A. Functional forms of 2D DFT of ellipse and diamond

A.1. Ellipse

According to the scaling property of Fourier transform,

$$F\left[f\left(\frac{x}{a},\frac{y}{b}\right)\right] = |ab|\cdot F(ua, vb) \tag{A.2}$$

For an ellipse, therefore, the Fourier transform is

$$F_E(u,v) = 2\pi R_1 R_2 \frac{J_1(\rho' R)}{\rho' R}, \quad \text{with } \rho' R = \sqrt{(R_1 u)^2 + (R_2 v)^2} \tag{A.3}$$

When $R_1 = R_2$, the Fourier transform is of the circular object.

A.2. Diamond

We now provide a derivation of the Fourier transform of a diamond-shaped binary image. Guasti et al. (*Int. J. Light Electron Opt.*, **116**, 2005: 265–269) give the Fourier transform of an intermediate shape between a circle and a square. Manuel et al. (*J. Opt. Soc. Am., A*, **21**, 2004: 1682–1689) reformulate Fourier transform of an ellipse using 2D Dirac delta curves. We consider the transition between a diamond and an ellipse to derive the Fourier transform of a diamond-shaped binary image. Consider the following expression:

$$\frac{x^2}{a^2} + \frac{y^2}{b^2} \pm c^2 xy = k^2 \tag{A.4}$$

If $c = 0$, it is an ellipse. If $c^2 = 2/ab$, it becomes a diamond. For $0 < c^2 < 2/ab$, (A.4) represents an intermediate shape between an ellipse and a diamond. When $c^2 \gg 2/ab$, the binary image becomes a pair of crossed lines. An ellipse becomes a circle when the two axes are equal. A diamond becomes a rectangle when $a = b$.

Let us calculate Fourier transform of a diamond-shape object. In the first and third quadrant of the frequency domain, Fourier transform of diamond can be obtained:

$$F_{D1}(u,v) = \frac{2ab}{au - bv}\left(-\frac{\cos(kbv) - 1}{bv} + \frac{\cos(kau) - 1}{au}\right) \tag{A.5}$$

Similarly, in the second and fourth quadrant, the Fourier transform is:

$$F_{D2}(u,v) = \frac{2ab}{au + bv}\left(\frac{\cos(kbv) - 1}{bv} + \frac{\cos(kau) - 1}{au}\right) \tag{A.6}$$

Thus we have the functional form of a diamond's Fourier transform:

$$F_D(u,v) = F_{D1}(u,v) + F_{D2}(u,v) \tag{A.7}$$

References

[1] S. Wang, Prediction of scattered sound field based on the reversal of acoustic diffraction tomography, in: The 17th International Congress on Sound and Vibration (ICSV17), Cairo, Egypt, 18–22 July, 2010.
[2] A.C. Kak, Malcolm Slaney, Principles of Computerized Tomographic Imaging, Society of Industrial and Applied Mathematics, Philadelphia, 2001.
[3] X. Zhao, Z. Wang, B. Liu, Phase aberration correction of ultrasonic phased array signals, Image and Signal Processing 5 (2008) 63–66.
[4] L. Zhu, Y. Xiong, B. Zhong, An approach for amplitude correction in line spectrum, Mechanical Systems and Signal Processing 17 (3) (2003) 551–560.
[5] K. Ding, X. Ming, Methods for amplitude, phase and frequency correction in discrete spectrum, Journal of Dynamic Analysis and Measurement 14 (1996) 10–29.
[6] N. Mueller, T.Q. Nguyen, Image interpolation using classification and stitching, in: Proceedings of the International Conference on Image Processing, ICIP 2008, October 12–15, 2008, pp. 901–904.
[7] L. Zhang, X. Wu, An edge guided image interpolation algorithm via directional filtering and data fusion, IEEE Transactions on Image Processing 15 (2006) 2226–2238.
[8] A. Ledda, H.Q. Luong, W. Philips, V. De Witte, E.E. Kerre, Binary image interpolation based on mathematical morphology, in: 16th European Signal Processing Conference (EUSIPCO 2008), Lausanne, Switzerland, August 2008, pp. 25–29.
[9] A. Averbuch, R.R. Coifman, D.L. Donoho, M. Israeli, Y. Shkolnisky, I. Sedelnikov, A framework for discrete integral transformations. II: The 2D discrete Radon transform, SIAM Journal on Scientific Computing 2 (30) (2008) 785–803.
[10] A.C. Kak, M. Slaney, Principles of Computerized Tomographic Imaging, IEEE Press, New York, 1999. pp. 56–75.
[11] L. Yang, Z. Huiyan, Shape preserving piecewise cubic interpolation, Applied Mathematics 11B (1996) 419–424.
[12] C.B. Mbachu, G.N. Onoh, V.E. Idigo, E.N. Ifeagwu, S.U. Nnebe, Processing ECG signal with Kaiser window-based FIR digital filters, International Journal of Engineering Science and Technology 3 (8) (2011) 6775–6783.
[13] S. Wang, Finite-difference time-domain approach to underwater acoustic scattering problems, Journal of the Acoustical Society of America 99 (4) (1996) 1924–1931. pt. 1.
[14] A. Averbuch, R.R. Coifman, D.L. Donoho, M. Elad, M. Israeli, Fast and accurate polar Fourier transform, Applied and Computational Harmonic Analysis 21 (2006) 145–167.